Depth dose measurements in water for C-11 and C-10 beams with therapy relevant energies

Boscolo, Daria; Kostyleva, Daria; Schuy, Christoph; Weber, Uli; Haettner, Emma; Purushothaman, Sivaji; Dendooven, Peter; Dickel, Timo; Drozd, Vasyl; Franczack, Bernhard

Link to publication in University of Groningen/UMCG research database

Citation for published version (APA):
Boscolo, D., Kostyleva, D., Schuy, C., Weber, U., Haettner, E., Purushothaman, S., Dendooven, P., Dickel, T., Drozd, V., Franczack, B., Geissel, H., Hornung, C., Horst, F., Kazantseva, E., Kuzminchuk-Feuerstein, N., Lovatti, G., Mukha, I., Nociforo, C., Pietri, S., ... Durante, M. (2022). Depth dose measurements in water for C-11 and C-10 beams with therapy relevant energies. *Nuclear instruments & methods in physics research section a-Accelerators spectrometers detectors and associated equipment*, *1043*, [167464]. https://doi.org/10.1016/j.nima.2022.167464

Depth dose measurements in water for ^{11}C and ^{10}C beams with therapy relevant energies

Daria Boscolo [a], Daria Kostyleva [a], Christoph Schuy [a], Uli Weber [a], Emma Haettner [a],
Sivaji Purushothaman [a], Peter Dendooven [b], Timo Dickel [a,c], Vasyl Drozd [a,d],
Bernhard Franczack [a], Hans Geissel [a,c], Christine Hornung [a,e], Felix Horst [a], Erika Kazantseva [a],
Natalia Kuzminchuk-Feuerstein [a], Giulio Lovatti [h], Ivan Mukha [a], Chiara Nociforo [a],
Stephane Pietri [a], Marco Pinto [h], Claire-Anne Reidel [a], Heidi Roesch [a,e], Olga Sokol [a],
Yoshiki K. Tanaka [f], Helmut Weick [a], Jianwei Zhao [a,g], Christoph Scheidenberger [a,c],
Katia Parodi [h], Marco Durante [a,e,*]

[a] *GSI Helmholtzzentrum für Schwerionenforschung, Darmstadt, Germany*
[b] *University Medical Center Groningen, Groningen, Netherlands*
[c] *Justus-Liebig-Universität Gießen, Gießen, Germany*
[d] *University of Groningen, Groningen, Netherlands*
[e] *Technische Universität Darmstadt, Darmstadt, Germany*
[f] *RIKEN High Energy Nuclear Physics Laboratory, Wako, Japan*
[g] *Peking University, Beijing, China*
[h] *Ludwig-Maximilians-Universität München, Munich, Germany*

ARTICLE INFO

ABSTRACT

Owing to the favorable depth-dose distribution and the radiobiological properties of heavy ion radiation, ion beam therapy shows an improved success/toxicity ratio compared to conventional radiotherapy. The sharp dose gradients and very high doses in the Bragg peak region, which represent the larger physical advantage of ion beam therapy, make it also extremely sensitive to range uncertainties. The use of β^+-radioactive ion beams would be ideal for simultaneous treatment and accurate online range monitoring through PET imaging. Since all the unfragmented primary ions are potentially contributing to the PET signal, these beams offer an improved image quality while preserving the physical and radiobiological advantages of the stable counterparts. The challenging production of radioactive ion beams and the difficulties in reaching high intensities, have discouraged their clinical application. In this context, the project Biomedical Applications of Radioactive ion Beams (BARB) started at GSI (Helmholtzzentrum für Schwerionenforschung GmbH) with the main goal to assess the technical feasibility and investigate possible advantages of radioactive ion beams on the pre-clinical level. During the first experimental campaign ^{11}C and ^{10}C beams were produced and isotopically separated with the FRagment Separator (FRS) at GSI. The β^+-radioactive ion beams were produced with a beam purity of 99% for all the beam investigated (except one case where it was 94%) and intensities potentially sufficient to treat a small animal tumors within few minutes of irradiation time, $\sim 10^6$ particle per spill for the ^{10}C and $\sim 10^7$ particle per spill for the ^{11}C beam, respectively. The impact of different ion optical parameters on the depth dose distribution was studied with a precision water column system. In this work, the measured depth dose distributions are presented together with results from Monte Carlo simulations using the FLUKA software.

1. Introduction

The use of β^+-radioactive ion beams (RIB) such as ^{11}C and ^{10}C, for simultaneous range verification and treatment, could represent a major improvement for heavy ion therapy applications [1–3].

Such beams could help to overcome range uncertainties, one of the larger limitations of heavy ion therapy [5], while preserving the physical and radiobiological advantages of the respective stable ion beams, ^{12}C, which are already in use for clinical applications [6]. Heavy ion therapy demonstrated to be a very effective and precise
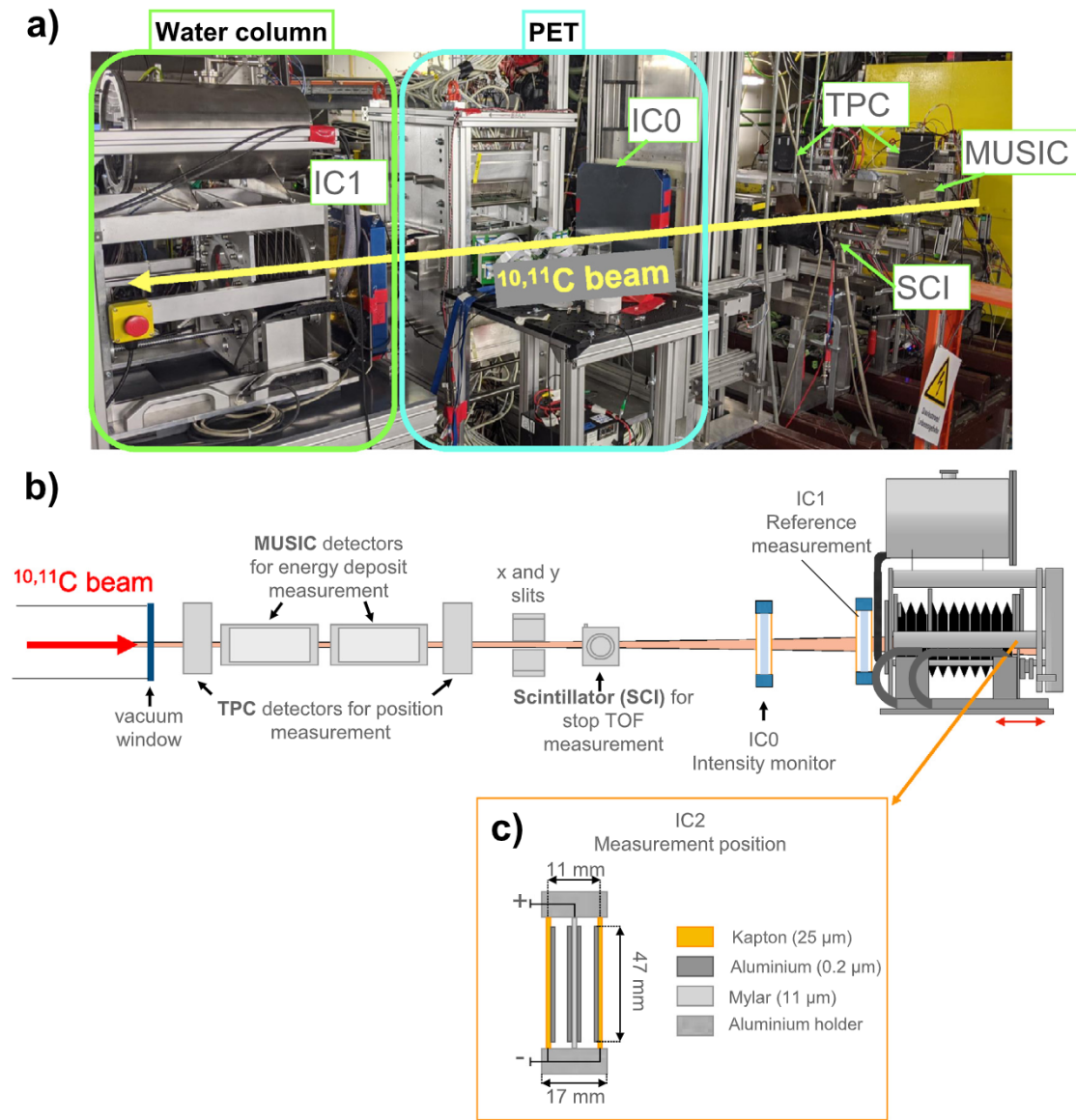

Fig. 1. Panel (a) Photo of the experimental set up located at the final focal plane of the FRS. Panel (b) Scheme of the setup at the final focal plane showing FRS standard particle-identification detectors and the water column setup for the depth dose measurement of ^{11}C and ^{10}C beams (not drawn to scale). Panel (c) Schematic structural design of the ionization chamber IC2 (adapted from [4]). Panel (b) and (c) not drawn to scale.

radiotherapy technique. However, the sharp dose gradients in the Bragg peak region makes it also extremely sensitive to range uncertainties caused by imaging, patient setup, beam delivery and dose calculation. Small shifts of the Bragg peak position can lead to large deviations in the dose deposition [7]. On the clinical level, to mitigate the effect of such uncertainties and guarantee the coverage of the tumor, margins extending in the healthy tissue are added to the target volume [8]. Range verification techniques have the potential to reduce these margins and provide an online treatment verification. For these reasons, an extensive effort has been made to investigate several possible range verification techniques [9]. Among them, Positron Emission Tomography (PET) has been tested most extensively in clinical practice [10] and allows a visualization of the beam by exploiting β^+-emitting isotopes. This β^+ activity can either come from projectile (in the case of heavy ion beams) and target fragments or, in the case of RIB, directly from the decay of the implanted primary ions. However, the capabilities of PET imaging applications in solving the issue of range uncertainties are still unsatisfactory, with a limit on the accuracy on range verification of about 2–5 mm, and its use for ^{12}C ion therapy remains marginal [1, 11–13].

The use of radioactive ion beams for simultaneous treatment and online treatment verification could be particularly advantageous. Compared to the stable ions, where β^+ isotopes are produced via fragmentation processes of the particle beam in the patient body, with RIB all the primary ions are potentially contributing to the PET signal and thus leading to an increased signal to noise ratio [14]. This, together with the short half-lives of the radioisotopes (20.33 min for ^{11}C and 19.3 s for ^{10}C), allows to reduce the time required to collect the PET signal, opening the possibility of an online range monitoring and also reducing the biological washout of the PET signal [15,16]. Additionally, differently than in the case of stable beams, with RIB the activity peak matches the mean ranges of the primaries and is correlated with the 80% distal fall-off after the Bragg peak (and almost coincides with the peak position in case of negligible beam momentum spread) [17].

However, even though the advantages of RIB are known for a long time [1], the difficulties in producing RIB with sufficiently high intensities, limited their application for clinical and pre-clinical studies. New developments at accelerator facilities such as the recent intensity upgrade of the SIS-18 accelerator at GSI (Darmstadt, Germany)
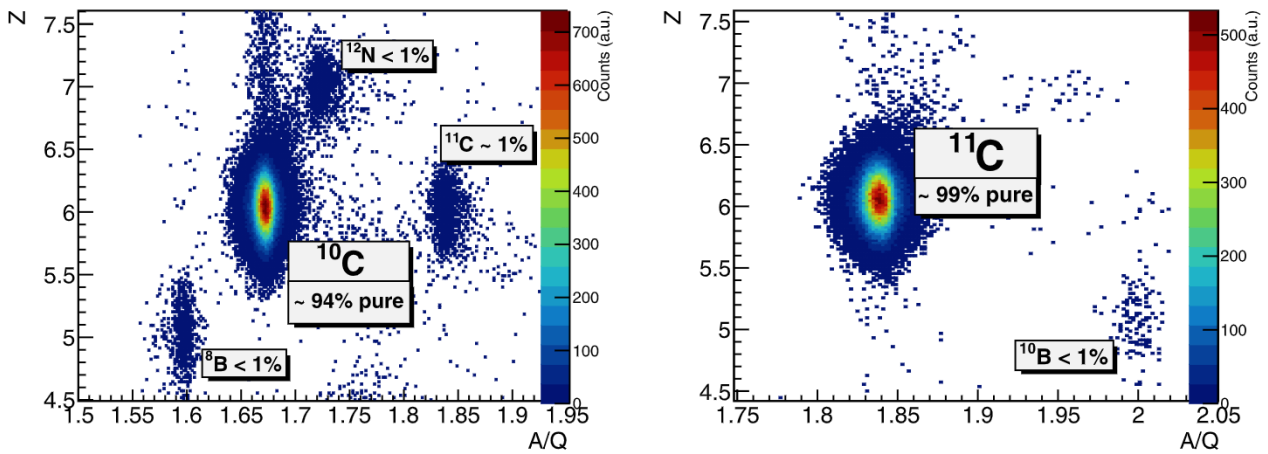
Fig. 2. Particle identification plots: atomic number Z vs. mass-over-charge ratio A/Q of the ions produced by the FRS. Panel (a) Identification of ^{10}C beam produced with 380 MeV/u ^{12}C primary beam energy. Panel (b) Identification of ^{11}C beam produced with 380 MeV/u ^{12}C primary beam energy.

towards the construction of FAIR [18], renewed the interest for RIB pre-clinical applications [19]. In this context, the Biomedical Applications of Radioactive ion Beams (BARB) project was funded by the European Research Council (ERC) in 2020, with the main objective of resuming previous studies with PET imaging of RIB at GSI and testing their application in-vivo [1,20,21]. Within this context, ^{11}C and ^{10}C beams were produced and isotopically separated with the FRagment Separator (FRS) at GSI and transported to the experimental vault at main branch of the FRS. The RIB were characterized in terms of momentum spread, purity and beam spot size and the impact of different ion optics on the depth dose distribution of the different PET isotopes was studied with a water column system. The performed measurements were complemented by a parallel experiment with two independent PET imaging setups visualizing the beam implantation in plastic targets: 1/6 of a Siemens Biograph mCT clinical positron emission tomography (PET) scanner [22] with custom-modified detectors and a prototype high resolution small animal PET detector being developed within the SIRMIO project [23,24]. The spatial resolution of the new system will be smaller than 1 mm, this result is achieved with 0.9 mm crystals and a wide angle coverage due to the spherical design of the detector. A description of the imaging systems used within the project can be found in [20]. Results from the imaging systems are not within the scope of this contribution and will be presented in separate works. In this contribution, the beam characterization and the measured depth dose distributions for two energies, in a therapy relevant range, and corresponding FLUKA [25–28] simulations are presented.

2. Material and methods

2.1. Production and identification of RIB with the FRS

The FRS is an in-flight separator and a magnetic spectrometer for the exotic radioactive beams with magnetic rigidities up to $B\rho = 18$ Tm [29]. The separator has a length of about 75 m and consists of four magnetic dipole sections. Each section has a dipole magnet which bends the passing beam by 30°, quadrupole magnets to focus/defocus the beam and hexapoles to introduce the ion-optical corrections. The ion-optical system of the FRS has four focal planes corresponding to each dipole section. The detector setup, described in this section, was located at the central and final focal planes of the main branch. The FRS was operated in a mono-energetic and an overall-achromatic ion-optical modes. The latter is a standard mode of the FRS operation, and has an emittance of 20 π mm mrad and a momentum spread of ±1%.

The radioactive beams of interest, namely ^{11}C and ^{10}C isotopes, were produced and spatially-separated by the FRS as follows. The primary beam of ^{12}C stable nuclei with the energies of 380 and 290 MeV/u

and intensities up to $\sim 4 \times 10^9$ particles per spill (spill length 2 s) were provided by the combination of the UNILAC [30] and SIS18 [31] accelerators of GSI. The beam interacted with the 8 g/cm^2 ^{9}Be primary target located at the entrance of the FRS where a variety of isotopes, including the ones of interest, was produced in a fragmentation reaction. The separation of the fragments was done by the $B\rho - dE - B\rho$ method [29]. The first two dipole stages performed the initial spatial separation of the fragments with a certain magnetic rigidity. In the central focal plane, a wedge-shaped degrader was placed in which different isotopes of the same rigidity lose different amount of energy. The latter allows a second round of $B\rho$ separation to be carried out with the remaining two dipole sections.

For an event-by-event particle identification, the second half of the FRS is used as a spectrometer in combination with the various standard particle detectors providing position, energy deposition dE and the velocity via time-of-flight (ToF) measurement, see e.g. [32]. By using these values, the mass-over-charge ratio, A/Q, and the atomic number, Z, can be evaluated and used to uniquely identify all the particles arriving at the final focus. Namely, the ToF was measured with two plastic scintillation detectors located at the central and final focii. The achieved time resolution for carbon isotopes is 120 ps. The ion charge was deduced from the energy deposition measured by the Multi-Sampling Ionization Chamber (MUSIC) [33] with a resolution of about 2%. The $B\rho$, and thus the position measurements were performed by Time Projection Chambers (TPC) detectors also located at both focii. The TPC resolution is about 0.2 mm [34]. Position measurements and subsequent tracking also provide the angular distributions of the secondary beams. The momentum spread of the beam is calculated as the difference between the measured positions at the central and final focal planes accounting on the magnification of the beam and divided by the dispersion coefficient. The scheme of the identification detectors at the final focal plane of the FRS together with the water column setup is shown in Fig. 1(a) and (b).

The achromatic and mono-energetic modes of the FRS operation were achieved by changing the slope of the 737 mg/cm^2 aluminum disk degrader located at the central focal plane. For the mono-energetic mode, the slope of the degrader is set to reduce the momentum spread of the selected fragment, but at the cost of a larger beam-spot size in the lateral direction at the final focal plane [35,36]. Here, the momentum spread can be reduced to a value comparable with the one of the primary beam ($\Delta p/p = 5 \times 10^{-4}$) [36]. On the contrary, the achromatic degrader preserves the overall ion-optical achromatism, and the beam is focused on the same spot at the final focus regardless of the initial angular and momentum spread.

Due to nuclear and atomic effects in the production target (such as energy loss straggling and multiple scattering) the secondary beams
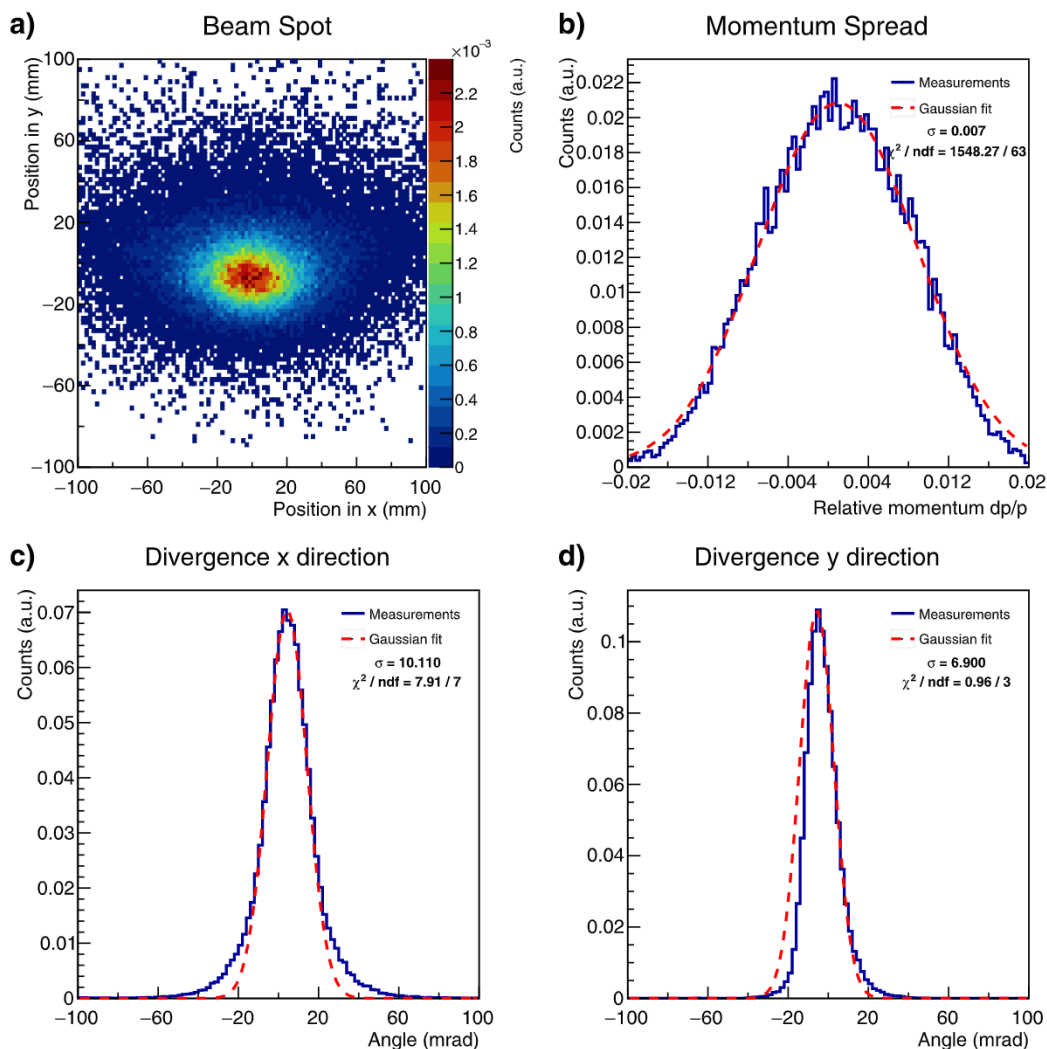
Fig. 3. Measured beam parameters for the ^{10}C beam, produced with the 290 MeV/u ^{12}C primary beam, in the achromatic ion optical mode. Panel (a) beam spot. Panel (b) momentum spread distribution. Panels (c) and (d) beam angular distribution in x and y direction, respectively. All the plots are normalized to the total number of entries. The fitting parameters are reported in Table B.4. Fits optimized in the range $\pm\sigma$ for the divergence in x and y direction and $\pm 2\sigma$ for the momentum spread.

produced at the FRS have a larger phase-space compared to the primary beam. This leads to a large relative momentum spread and, thus, in a less sharp Bragg peak compared to the primary beam, see further sections for details.

For the depth-dose measurements, the thickness of a homogeneous degrader located at central focal plane was tuned such that the secondary ^{10}C and ^{11}C beams, produced from a ^{12}C of 390 and 280 MeV/u, have a similar range in water: ~12 and ~4.5 cm respectively. The impact of the two ion-optical modes on the depth dose distribution was studied for ^{10}C and ^{11}C beams for the two investigated energies.

2.2. Depth dose distribution measurements

For all produced RIB, depth dose distributions in water have been measured with a water column setup, which is a modified version of the setup described in [37,38], and consists of a water phantom of variable thicknesses placed in between two parallel-plate ionization chambers (ICs). The range of measurable water equivalent path lengths goes from 2.4 to 29 cm. The thickness of the water column is varied by a stepper motor and read out by an optical linear encoder with a relative precision of 10 μm. The front and back windows of the water phantom are made of 0.5 cm glass whose water equivalent thickness was previously characterized in terms of water equivalent path length to be 9.25 mm for each window.

The laterally integrated depth dose distribution is obtained from the ratio of the signals collected by the two ICs as a function of the water thickness. The first ionization chamber (IC1), placed in front of the water column, provides the reference signal. This chamber is a large area parallel plate IC with an active area of $24 \times 24 \times 2$ cm^3 operated with a mixture of ArCO$_2$ (80% Ar and 20% CO$_2$) (similar structure to [39]). To minimize the impact of air gaps on the depth dose measurements, the IC1 is placed as close as possible to the front of the water column. The second ionization chamber (IC2), which provides a signal correlated to the energy loss behind the water target, is a parallel plate IC with an active area of 4.7 cm diameter and operated in air (this chamber is a GSI construction based on the parallel-plate ionization chamber TM233612/U901-0319 by PTW). A schematic structural design of the IC2 is shown in Fig. 1(c), more details can be found in [4]. The IC2 was placed in a dedicated holder attached to the back glass window of the water column and moved together with it.

The readout of both ICs was done with high-precision electrometers (model K6517, KEITHLEY), with an accuracy of the charge measurement in the order of 1‰. A schematic of the water column setup is shown in Fig. 1(a) and (b).

2.3. FLUKA simulations

Monte Carlo simulations were performed with the FLUKA code (version 2020.1.10) [25–28] in combination with the graphical user
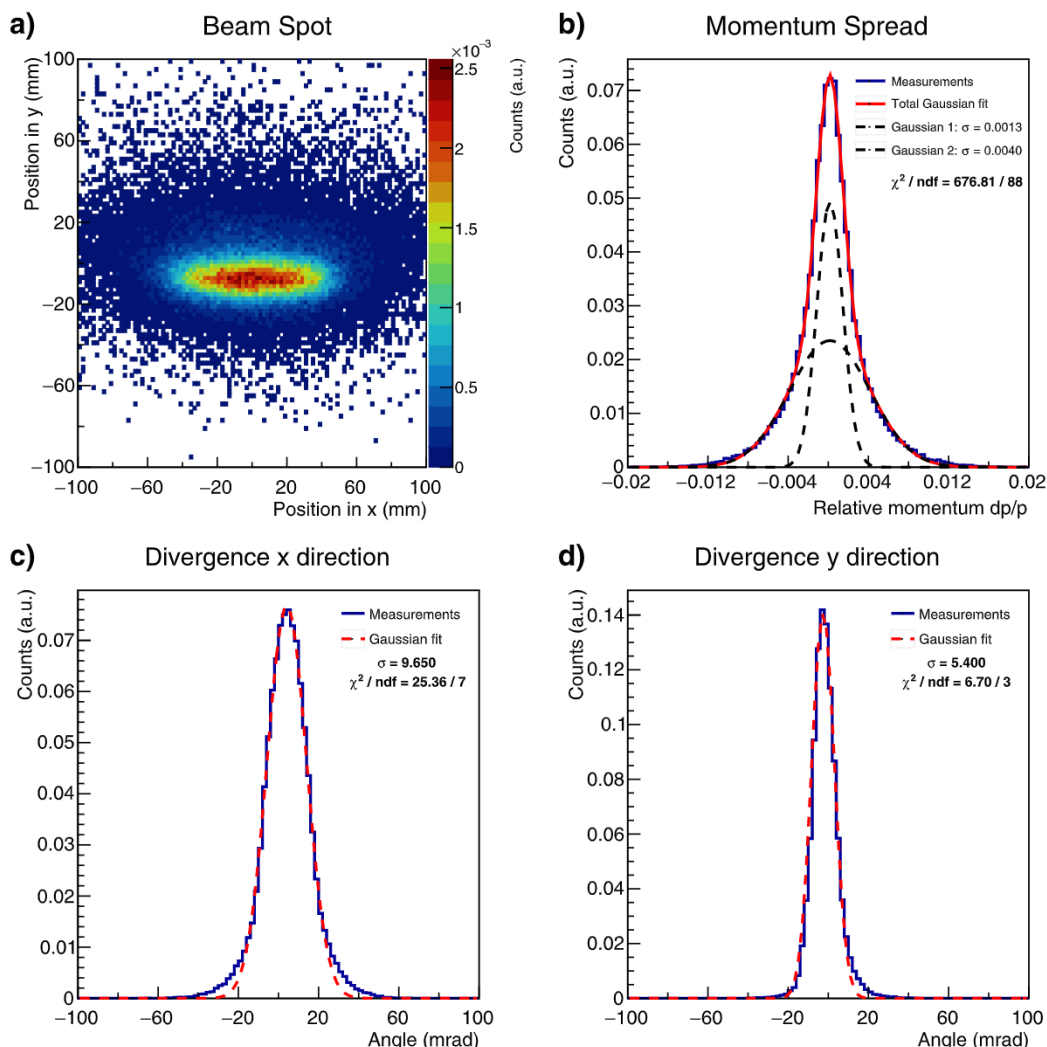
Fig. 4. Measured beam parameters for the ^{11}C beam, produced with the 380 MeV/u ^{12}C primary beam, in the mono-energetic ion optical mode. Panel (a) beam spot. Panel (b) momentum spread distribution. The double Gaussian fit (in red) together with the contribution of the two independent Gaussian functions is here shown, for the simulation only the width of Gaussian 1 was used. Panels (c) and (d) beam angular distribution in x and y direction, respectively. All the plots are normalized to the total number of entries. The fitting parameters are reported in Table B.1. Fits optimized in the range $\pm\sigma$ for the divergence in x and y direction and $\pm 2\sigma$ for the momentum spread.

interface flair (version 2.3-0) [40]. All the simulations were performed using the HADROTHErapy DEFAULT card, which is recommended for particle therapy applications. The water column was approximated by a water cylinder of 20 cm diameter, neglecting the glass windows but considering their water equivalent thickness. For all simulations the mean water ionization potential was set to 78 eV, according to the ICRU 90 report [41]. The IC1 was modeled as a $24 \times 24 \times 2$ cm^3 ArCO$_2$ scoring volume between two Mylar windows of 25 μm. The IC2 was represented as a cylindrical scoring volume of 4.7 cm diameter and 1.1 cm thickness filled with air surrounded by the aluminum frame and the two 25 μm Kapton windows. In order to take into account the reduced acceptance of the IC2, individual simulations were performed for each different depth in water, i.e. the dose in the active volumes of the ionization chambers was scored with the USRBIN card (a standard scorer in FLUKA) for each water thickness. The same simulation approach was also used in [38,42].

As the phase-space of secondary beams can significantly differ from the one of the primary ion beam, and in order to take into account the different beam characteristics for the investigated ion optical modes, a customized user routine was used to better describe the specific beam parameters. In particular, this new SOURCE routine can simulate beams with a double Gaussian beam spot distribution in x and y directions, a double Gaussian momentum spread distributions and a Gaussian

divergence distribution with different FWHMs in x and y directions. All the above mentioned beam parameters, have been obtained by fitting the measured data.

3. Results and discussion

Secondary beams were produced at the FRS and their intensities, measured with a calibrated ionization chamber (IC1) at the entrance of the water column, reached $\sim 10^6$ particle per spill for ^{10}C and $\sim 10^7$ particle per spill for ^{11}C beams. The production cross section, in the energy range covered during this experiment, is about an order of magnitude larger for ^{11}C compared to ^{10}C [43].

A beam purity of 99% was achieved for most of the cases, except for the ^{10}C beam, produced by a 380 MeV/u ^{12}C primary beam where the beam purity was 94%. Note that the ^{10}C purity could easily be improved by using a thicker degrader at the mid-focal plane. During the experiments, for time reasons, the condition of same range in water for the different isotopes were achieved varying the degrader thickness, thus leading to not optimal purity for this secondary beam. The purity of the ^{10}C and ^{11}C secondary beams achieved in this experiment as well as the intensities of the beams at the final focal plane are presented in the Table 1. Please note that the measured beam purity reflects the beam composition at the entrance of the experimental cave. Due
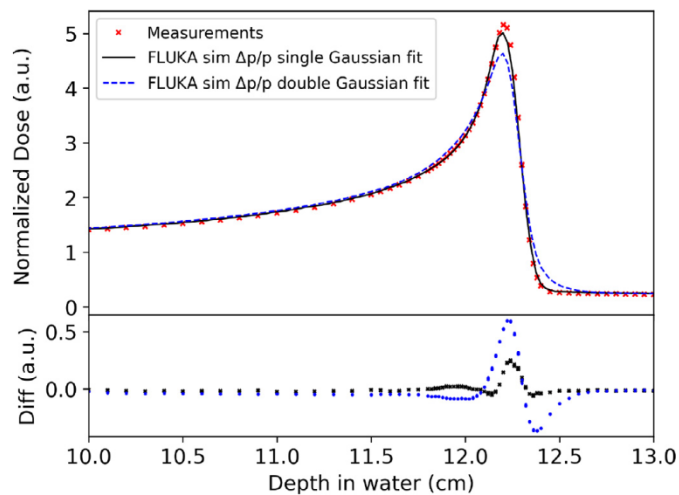
Fig. 5. Impact of the momentum spread distribution on the simulated Bragg peak shape for ^{11}C beam, produced with the 380 MeV/u ^{12}C primary beam in the mono-energetic mode. Measured data are represented with red crosses, while the black solid and blue dashed lines show the FLUKA simulation results when the momentum spread distribution is described using a single Gaussian and a double Gaussian fit of the experimental data respectively. The fitting curves together with the respective fitting parameters used to describe the momentum spread are shown in Fig. 4b. To better appreciate the deviations of the simulated data compared to the measurements the difference between the two curves is reported below the depth dose distribution.

to fragmentation reaction in the detector set up and in the air gaps we estimate that 3%–4% of the ions of interest will still undergo fragmentation processes before entering the water column system. As an example, the measured particle identification plots for ^{10}C and ^{11}C beams produced with a 380 MeV/u ^{12}C primary beam are shown in Fig. 2(a) and (b), correspondingly. The purity of the fragments is indicated on the same plot.

As mentioned in Section 2.1 the beams spot size, momentum spread and angular distributions were measured. The measured momentum spread $\Delta p/p$, position and angular distributions of the fragments of interest are shown in Figs. 3 and 4 for an achromatic ^{10}C beam, produced with a 290 MeV/u ^{12}C primary beam, and for a mono-energetic ^{11}C beam, produced with a 380 MeV/u ^{12}C primary beam, correspondingly. For all the other beam configurations, the measured beam parameters are reported in Appendix A.

The measured angular direction, the beam spot shapes and the momentum distribution, were parametrized, for all the investigated beams, through a fitting process. The fitting parameters were also used for the beam description in the Monte Carlo simulations and are reported in Appendix B, as they were used in the simulations. For all the beams, the angular direction and the beam spot shapes were fitted with a single Gaussian distribution, except for some beam spot shapes which were found to be better described by the sum of two Gaussian distributions. A single Gaussian distribution was used to fit the momentum spread distribution of the lower energy ^{10}C and ^{11}C beams in achromatic mode. For all the other investigated conditions, the momentum spread distributions were fitted as a sum of two Gaussians and the width of the most populated one was used for the simulations, see Fig. 4(b). The second Gaussian was rejected because it was found that the more populated Gaussian alone better reproduce the measured depth dose distributions. This can easily be observed in Fig. 5, where the impact of different momentum spread distribution on the depth dose distribution is shown for the mono-energetic ^{11}C beams produced with a 380 MeV/u ^{12}C primary beam. Simulation results obtained using the single and double Gaussian parametrization of the momentum spread are presented together with measured data, the image focus on the Bragg peak region. Fit parameters for the single and double

Gaussian fit are reported in Fig. 4b. More details on the measured and simulated depth dose distribution will be provided later in the text.

The momentum spread distributions strongly differ between the achromatic and mono-energetic mode: it is sharper for the mono-energetic ion optical mode, see Figs. 3 and 4. As an example, in the case of ^{11}C beam, produced with a 380 MeV/u ^{12}C primary beam, the momentum spread (standard deviation) varied from $\Delta p/p = 0.13\%$ in the mono-energetic mode to $\Delta p/p = 0.42\%$ in the achromatic ion optical mode. Additionally, for the same ion optical setting, it is larger for the lower energy beams: in the mono-energetic ion optical mode $\Delta p/p$ was 0.13% and 0.25% (0.42% and 0.74% in the achromatic mode) for the ^{11}C beam produced with the 380 MeV/u and the 290 MeV/u ^{12}C beam, respectively. Large differences of the beam spot size along the x direction were observed between the achromatic and mono-energetic ion optical modes. While the beam spot in the achromatic mode has a more symmetric shape in x and y direction, in the case of mono-energetic ion optical mode the beam spot is elongated (see Fig. 4) in the x direction: reaching beam width of up to 8.7 cm FWHM, in the case of ^{10}C produced with a 290 MeV/u ^{12}C beam. For the case of mono-energetic ion optical mode the beam spot shape is not suitable for pre-clinical applications, especially for small animal tumors: due to the small size of the target volume the use of collimators would be necessary and, thus leading to a lower beam intensity on target. For all the studied RIB the beam divergence was found to be asymmetric in the x and y direction, with standard deviations of the beam angular distributions between 9.65 and 11.8 mrad along the x direction and between 5.4 and 7.25 mrad in along the y direction. These values are comparably large with respect to standard therapy settings, using stable primary beams, where beam divergences are in the order of few mrad.

The measured depth dose distribution curves (red crosses) for the different beams investigated in this work are shown, together with their FLUKA simulations (black lines), for the ^{10}C and ^{11}C beams in Figs. 6 and 7, respectively. The curve shown are normalized to the first measured position.

For better comparison, the difference between the measured data and simulation is shown in the bottom panels. All the measured curves were obtained with a minimum of 96 depth steps. The curves measured in the different ion optical modes are presented separately. As expected, due to the larger momentum spreads, the Bragg curves in the achromatic ion optical mode show broader and lower peak compared to the mono-energetic case. However, this does not represent a real limitation for clinical applications where, often, dedicated ripple filters (RiFi) are used to broaden momentum spread, and therefore the Bragg peak, in order to be able to irradiate the tumor with a uniform dose distribution and a reasonable number of energy steps [44]. Secondary beam energies were estimated with LISE++ (version 13.4.5 beta) [45], based on the measured path length in water and directly in FLUKA by matching the exact peak position. Estimated energies are reported together with the ranges, the achieved intensities and beam purity in Table 1. Ranges (defined by 80% of the maximum dose at the distal fall-off) are reported for the mono-energetic mode and in brackets for the achromatic mode.

FLUKA Monte Carlo simulations are shown together with the experimental results in Figs. 6 and 7. In order to take into account the small acceptance of IC2 (especially in the case of mono-energetic mode where the beamspot size along the x direction exceeds the maximum acceptance of the detector) the FLUKA simulations were performed in a step by step approach, i.e., for each depth dose curve, a minimum of 35 depth positions were simulated individually, with a coarser sampling in the entrance channel and in the tail and a more fine sampling in the Bragg peak region. The simulated curves, shown in Figs. 6 and 7, are obtained after interpolating the simulated points. In order to better appreciate the deviations of the simulated data compared to the measured one, the difference between the two curves is reported below the depth dose distributions. In all the cases large differences are shown in the Bragg curve fall-off region where, due to the high

Table 1

Beams energies, purity intensities and ranges (defined by 80% of the maximum dose at the distal fall-off) are reported for the mono-energetic mode and in brackets for the achromatic mode. Measured intensities have typical fluctuations in the order of 20%. Reported purity is within 1% for both achromatic and mono-energetic modes, however an additional fragmentation, up to 3%–4%, of the beam of interest is expected to take place between particle identification measurement position and the water column setup.

Primary beam			Secondary beams				
Ion	Intensity (pps)	Energy (MeV/u)	Ion	Energy (MeV/u)	Range in water (cm)	Intensity (pps)	Beam purity
^{12}C	4×10^9	290	^{11}C	146.0 ± 2.5	4.6 ± 0.1 (4.6)	1.2×10^7	98%
			^{10}C	155.0 ± 2.5	4.6 ± 0.1 (4.6)	0.7×10^6	99%
		380	^{11}C	258.0 ± 2.0	12.2 ± 0.1 (12.2)	2.0×10^7	99%
			^{10}C	272.0 ± 2.5	12.1 ± 0.1 (12.1)	1.2×10^6	94%[a]

[a]Note that the use of the purity of ^{10}C can easily be improved by using a thicker degrader at the mid-focal plane. For time reasons the condition of same range of different isotopes were achieved by variation of degrader thickness, thus leading to not optimal purity.
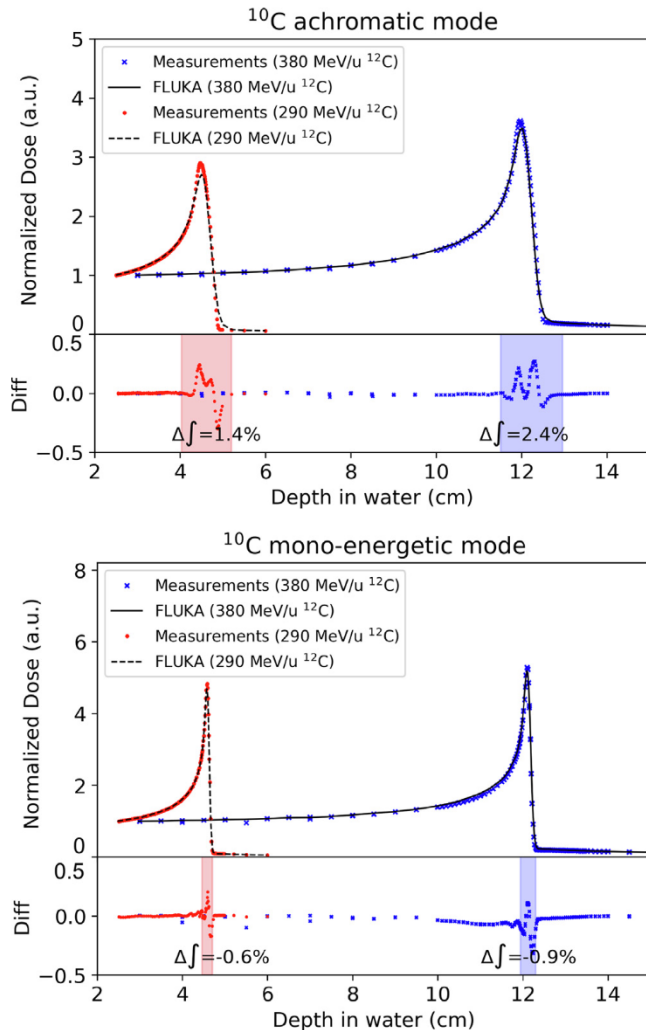

Fig. 6. Measured and simulated laterally integrated depth dose distribution curves in achromatic and mono-energetic optical mode for the ^{10}C beam. The curve are represented together with their respective difference and the deviation in the area under the peak (represented by the colored regions in the lower panel). In each Panel the curves obtained for the two different energies investigated are presented.

Fig. 7. Measured and simulated laterally integrated depth dose distribution curves in achromatic and mono-energetic optical mode for the ^{11}C beam. The curve are represented together with their respective difference and the deviation in the area under the peak (represented by the colored regions in the lower panel). In each Panel the curves obtained for the two different energies investigated are presented.

dose gradients, very small shifts in depth can lead to big deviations. However, when comparing the area under the peak – here defined as the area underlying the curve in the region between 60% and 5% of the maximal dose before and after the Bragg peak respectively – deviation ranging between 0.6% and 4.8% are observed.

In most cases, the FLUKA simulations underestimate the peak height except for the ^{11}C beam in achromatic mode. The observed deviations, between the measured and simulated depth dose distribution curves,
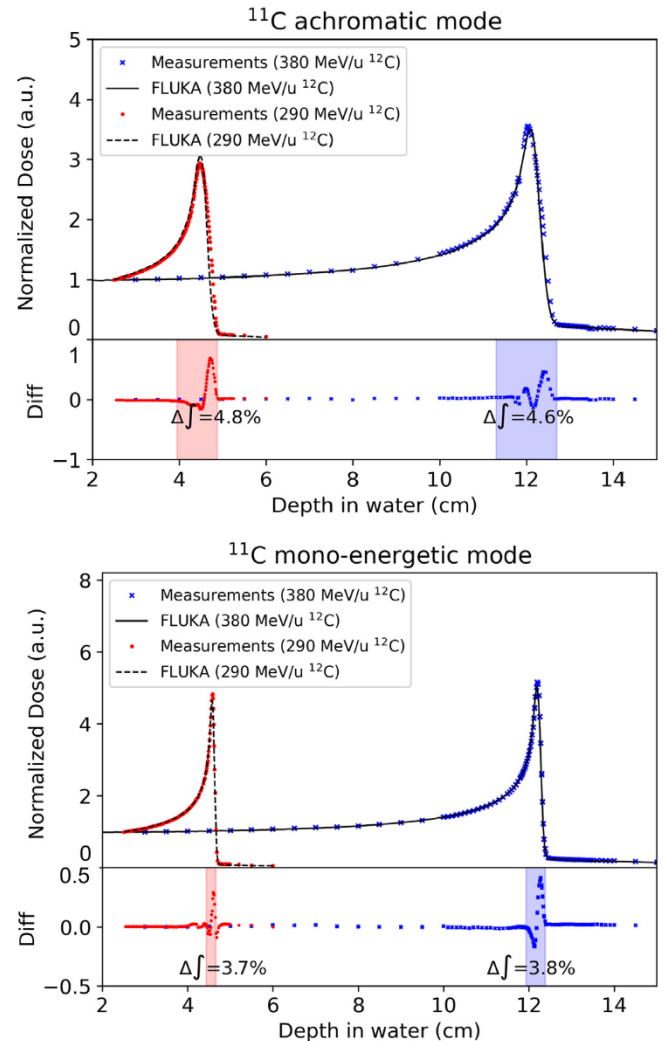
are most probably due to uncertainties on the total reaction cross section models in FLUKA or on the description of the beam parameters such as the momentum spread distribution. The contribution of possible inaccuracies in the simulated geometry, such as the simplification of the target (where the glass windows are not explicitly included) or differences in the air gaps, have been excluded by performing a sensitivity analysis in a cylindrical water target with radius equal to IC2 similar to the one presented in [42].

Also, the small acceptance of IC2 leads to a non negligible sensitivity of the scored energy deposition to the angular distribution of the fragments [4], which is more complicated for Monte Carlo codes to predict compared to the total yield. This can also explain the slight underestimation of the fragmentation tail by the FLUKA code observed for all the cases.

4. Conclusions

β^+-radioactive carbon ion beams with the therapy-relevant energies ^{11}C and ^{10}C, were produced and separated by the FRS fragment separator using two different ion-optical modes of the separator operation. Thanks to the upgrade of the SIS-18 accelerator within the framework of the FAIR project, it was possible to achieve RIB intensities potentially sufficient to treat small animal tumors, $\sim 10^6$ particle per spill for ^{10}C and $\sim 10^7$ particle per spill for ^{11}C beam, respectively. A beam purity of the 99% was achieved for all the beams, with the exception the ^{10}C, produced with a 380 MeV/u primary beam, where the beam purity was 94%. The impact of different ion optical modes on the depth dose distribution in water was studied for ^{11}C and ^{10}C beams at the main branch of the FRS. Depth dose distributions in water were measured (for all the investigated conditions) with a water column setup and compared to FLUKA simulations. Monte Carlo simulations succeeded to well reproduce the measured Bragg curve shapes and show deviations in the areas under the peak ranging between 0.6% and 4.8%, demonstrating that the FLUKA code provides reliable results for ^{11}C and ^{10}C beams in the therapy energy range. The data of this study are the first experimental results within the framework of the BARB project, and provide basic information necessary for range verification and for correlating dose deposition maps with the PET signals, which have been measured during this experimental campaign and will be presented in a separate work. Additionally, the measured beam parameters such as angular beam distribution, lateral profiles and energy spread are required as input in transport codes, treatment planning and radiobiological models which will be used for future experiments.

Declaration of competing interest

The authors declare the following financial interests/personal relationships which may be considered as potential competing interests: Marco Durante reports financial support was provided by European Research Council.

Data availability

Data will be made available on request.

Appendix A. Measured beam characteristics

See Figs. A.8–A.13.

Fig. A.8. Measured beam parameters ^{11}C beam, produced with the 380 MeV/u primary beam, in the achromatic ion optical mode. Panel (a) beam spot. Panel (b) momentum spread distribution. Panels (c) and (d) beam angular distribution in x and y direction, respectively. All the plots are normalized to the total number of entries. The fitting parameters are reported in Table B.1. Fits optimized in the range $\pm\sigma$ for the divergence in x and y direction and $\pm2\sigma$ for the momentum spread.
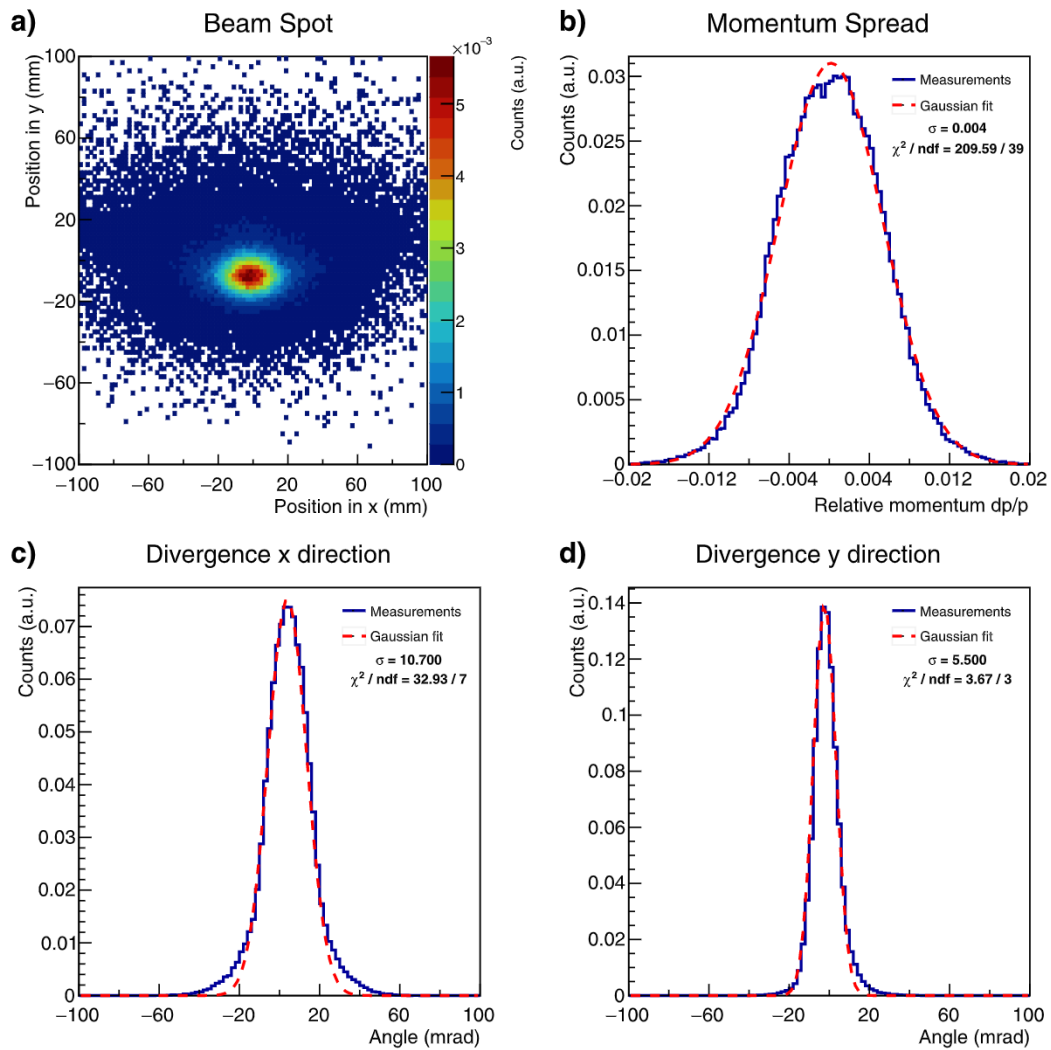
Fig. A.9. Measured beam parameters ^{11}C beam, produced with the 290 MeV/u primary ^{12}C beam, in the achromatic ion optical mode. Panel (a) beam spot. Panel (b) momentum spread distribution. Panels (c) and (d) beam angular distribution in x and y direction, respectively. All the plots are normalized to the total number of entries. The fitting parameters are reported in Table B.2. Fits optimized in the range $\pm\sigma$ for the divergence in x and y direction and $\pm 2\sigma$ for the momentum spread.

Fig. A.10. Measured beam parameters ^{11}C beam, produced with the 290 MeV/u primary ^{12}C beam, in the mono-energetic ion optical mode. Panel (a) beam spot. Panel (b) momentum spread distribution. Panels (c) and (d) beam angular distribution in x and y direction, respectively. All the plots are normalized to the total number of entries. The fitting parameters are reported in Table B.2. Fits optimized in the range $\pm\sigma$ for the divergence in x and y direction and $\pm 2\sigma$ for the momentum spread.
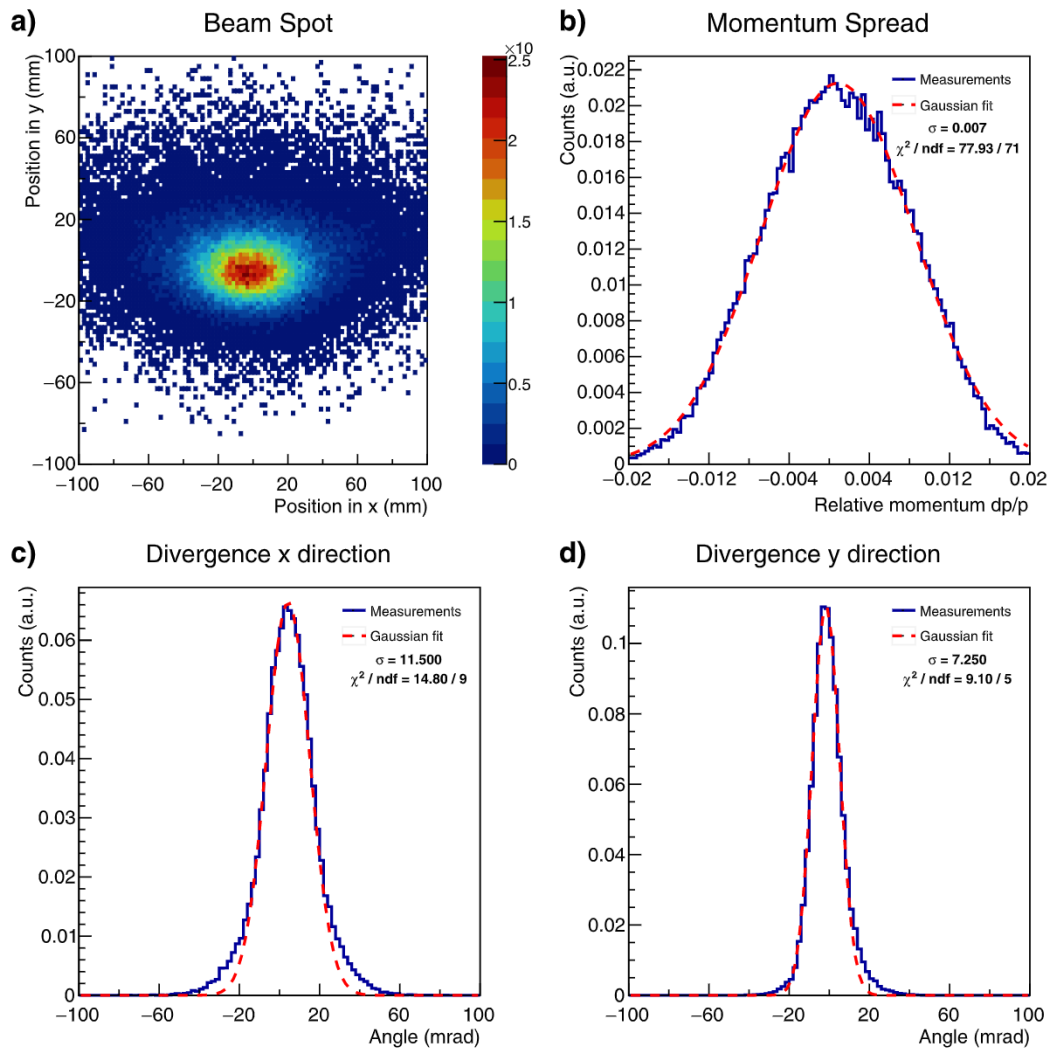
Fig. A.11. Measured beam parameters ^{10}C beam, produced with the 380 MeV/u primary ^{12}C beam, in the achromatic ion optical mode. Panel (a) beam spot. Panel (b) momentum spread distribution. Panels (c) and (d) beam angular distribution in *x* and *y* direction, respectively. All the plots are normalized to the total number of entries. The fitting parameters are reported in Table B.3. Fits optimized in the range $\pm\sigma$ for the divergence in *x* and *y* direction and $\pm 2\sigma$ for the momentum spread.
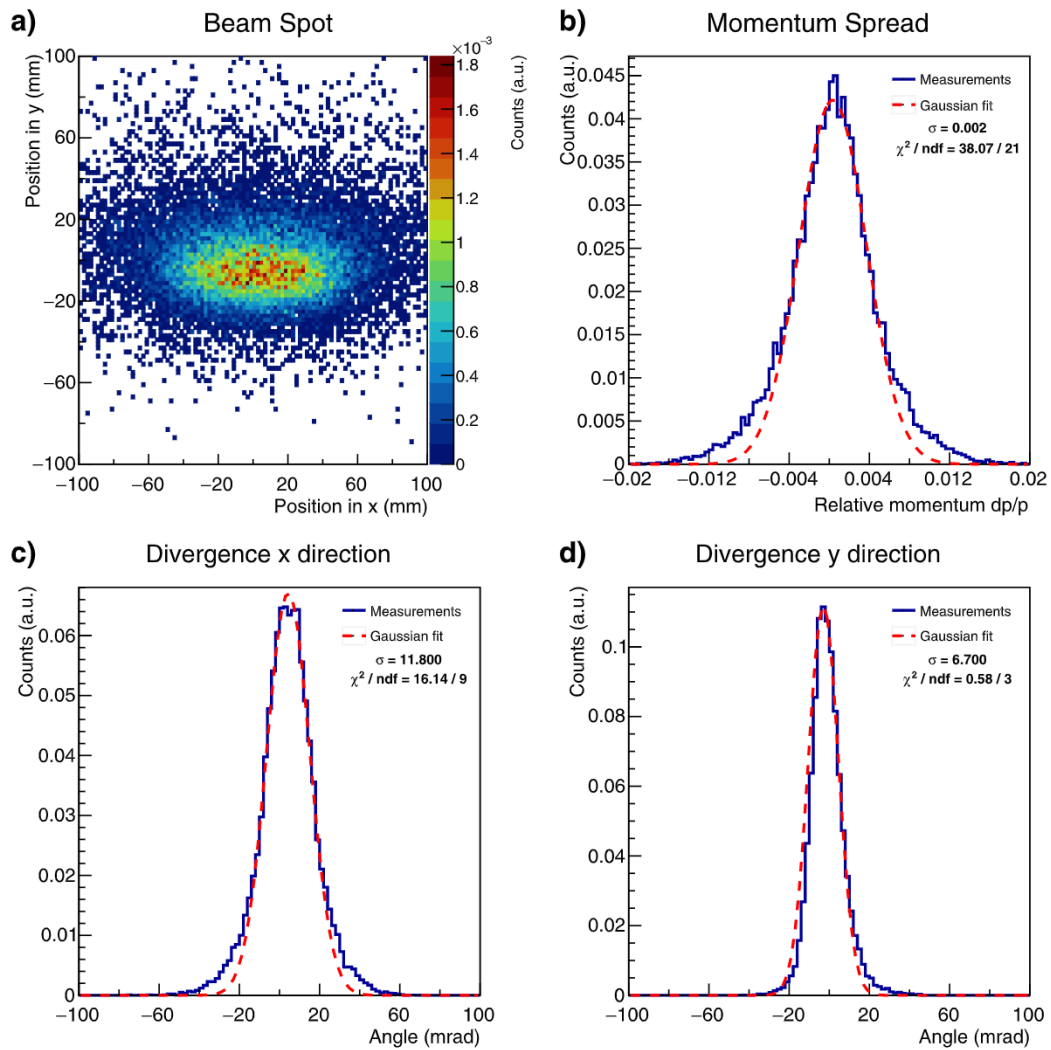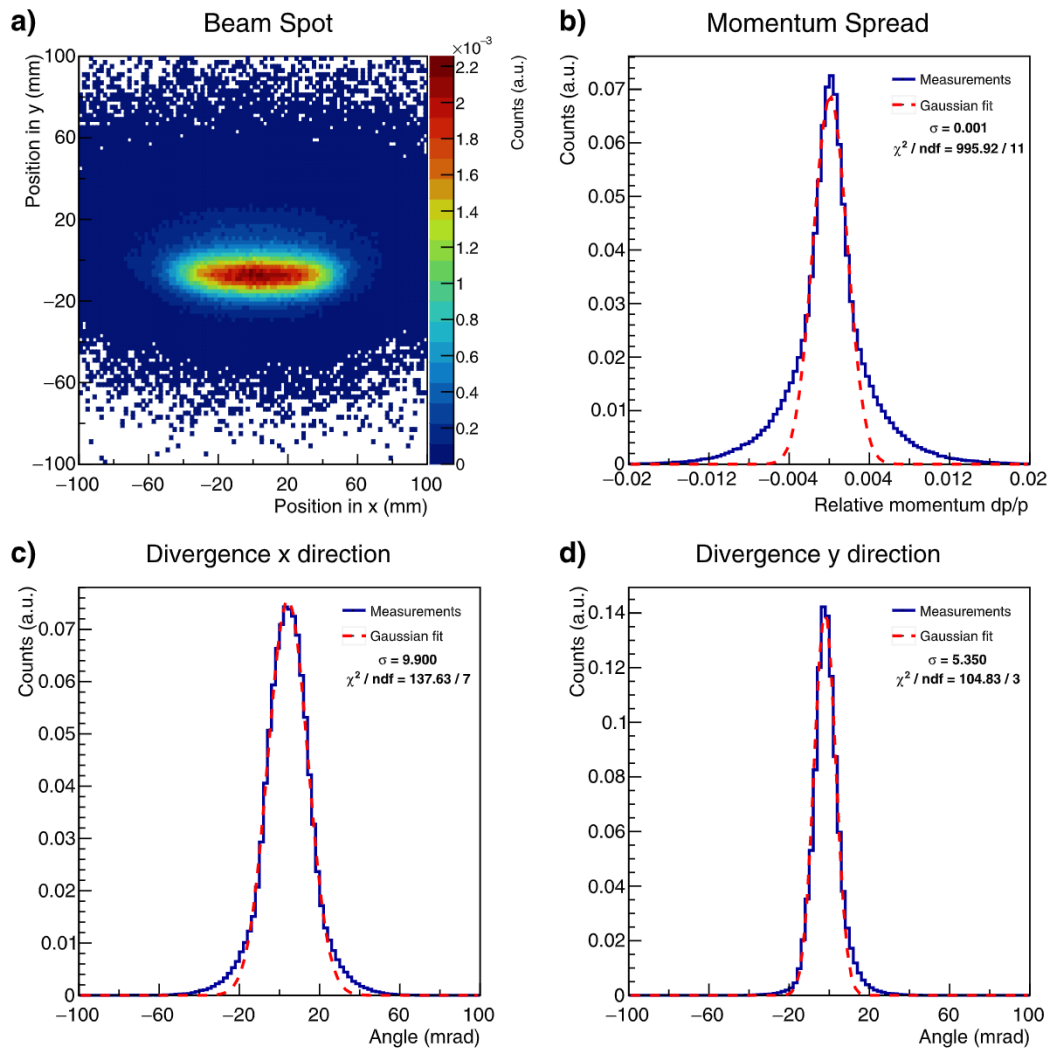
Fig. A.12. Measured beam parameters ^{10}C beam, produced with the 380 MeV/u primary ^{12}C beam, in the mono-energetic ion optical mode. Panel (a) beam spot. Panel (b) momentum spread distribution. Panels (c) and (d) beam angular distribution in x and y direction, respectively. All the plots are normalized to the total number of entries. The fitting parameters are reported in Table B.3. Fits optimized in the range $\pm\sigma$ for the divergence in x and y direction and $\pm2\sigma$ for the momentum spread.
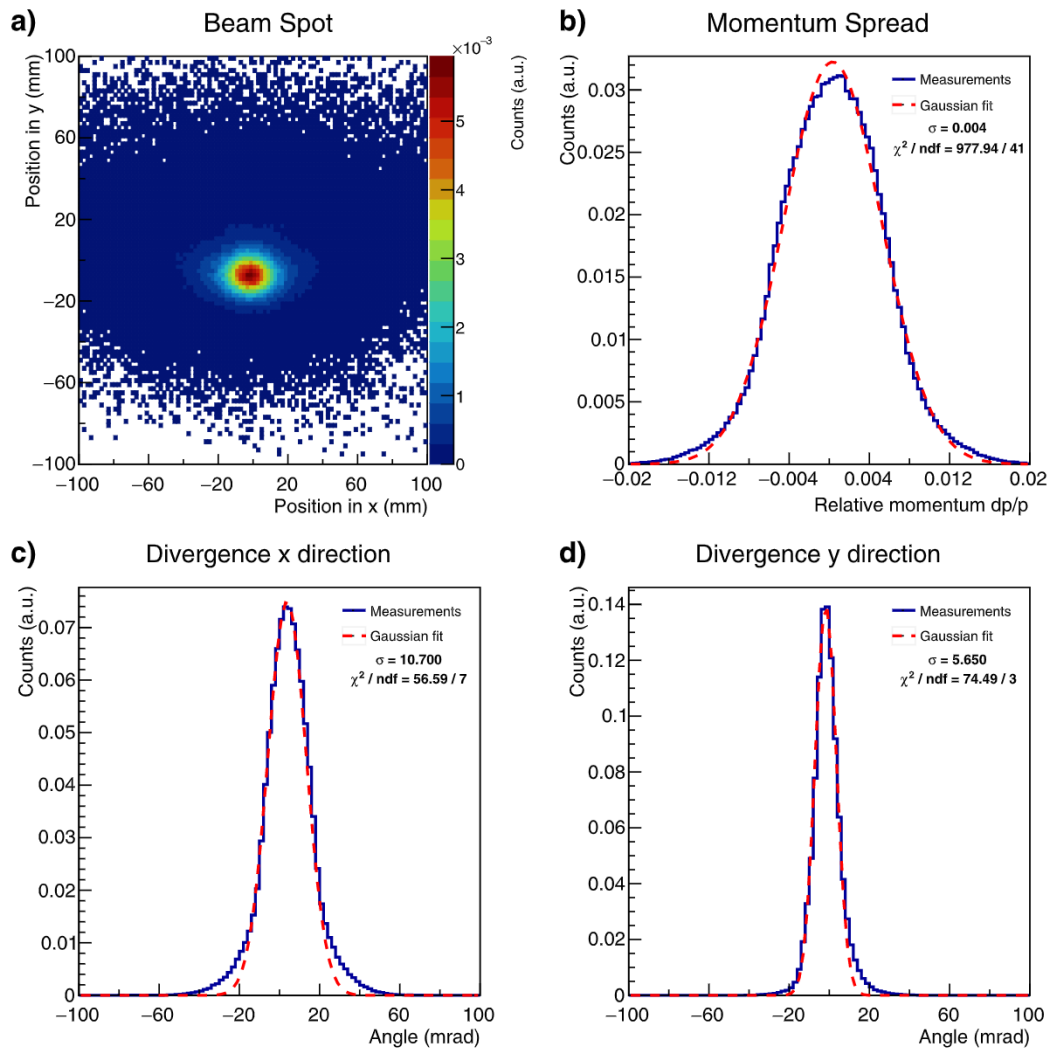
Fig. A.13. Measured beam parameters ^{10}C beam, produced with the 290 MeV/u primary ^{12}C beam, in the mono-energetic ion optical mode. Panel (a) beam spot. Panel (b) momentum spread distribution. Panels (c) and (d) beam angular distribution in *x* and *y* direction, respectively. All the plots are normalized to the total number of entries. The fitting parameters are reported in Table B.4. Fits optimized in the range $\pm\sigma$ for the divergence in *x* and *y* direction and $\pm 2\sigma$ for the momentum spread.
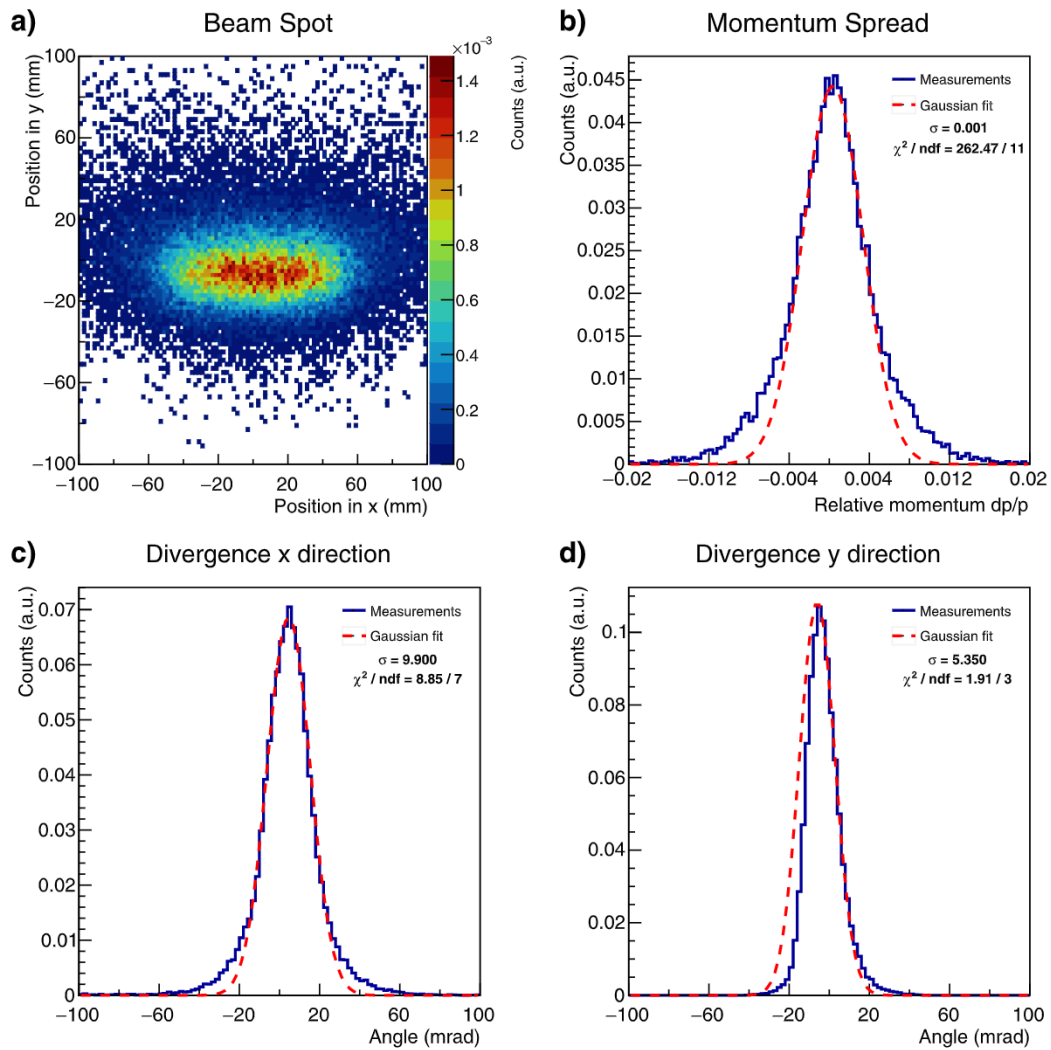
Table B.1
Beam spot size, momentum distribution and beam divergence parameters used in the FLUKA simulation of the ^{11}C beam of 258 MeV/u in achromatic and mono-energetic mode. The standard deviation is here reported for all the quantities that were described with a single Gaussian distribution. In the cases where the beam spot shape was better described as a double Gaussian distribution, the weighting factors ($a_{1,2}$), mean values ($m_{1,2}$) and the standard deviations ($\sigma_{1,2}$) of the two Gaussian curves are reported.

		^{11}C 258 MeV/u mono-energetic mode		
Beam spot size x (cm)	Beam spot size y (cm)	$\Delta p/p$ (%)	Divergence x (mrad)	Divergence y (mrad)
3.2	a_1= 0.80 m_1= −0.6 σ_1= 0.6 a_2= 0.20 m_2= 0.1 σ_2= 1.7	0.13[a]	9.6	5.4

		^{11}C 258 MeV/u Achromatic mode		
Beam spot size x (cm)	Beam spot size y (cm)	$\Delta p/p$ (%)	Divergence x (mrad)	Divergence y (mrad)
a_1 = 0.76 m_1 = −0.2 σ_1 = 1.0 a_2 = 0.24 m_2 = 0.0 σ_2 = 3.1	a_1 = 0.80 m_1 =-0.7 σ_1 = 0.7 a_2 = 0.20 m_2 = 0.0 σ_2 = 1.7	0.42[a]	10.7	5.5

[a]The experimental data were fitted as the sum of two independent Gaussian functions. For the simulation only the width of the more populated one (here reported) was used.

Table B.2
Beam parameters used for the FLUKA simulation of the ^{11}C beam of 146 MeV/u in achromatic and mono-energetic mode. The standard deviation is here reported for all the quantities that were described with a single Gaussian distribution. In the cases where the beam spot shape was better described as a double Gaussian distribution, the weighting factors ($a_{1,2}$), mean values ($m_{1,2}$) and the standard deviations ($\sigma_{1,2}$) of the two Gaussian curves are reported.

		^{11}C 146 MeV/u mono-energetic mode		
Beam spot size x (cm)	Beam spot size y (cm)	$\Delta p/p$ (%)	Divergence x (mrad)	Divergence y (mrad)
3.5	1.2	0.25[a]	11.8	6.7

		^{11}C 146 MeV/u Achromatic mode		
Beam spot size x (cm)	Beam spot size y (cm)	$\Delta p/p$ (%)	Divergence x (mrad)	Divergence y (mrad)
a_1 = 0.70 m_1 = −0.4 σ_1 = 1.8 a_2 = 0.30 m_2 = −0.1 σ_2 = 4.2	a_1 = 0.74 m_1 = −0.5 σ_1 = 1.0 a_2 = 0.26 m_2 = 0.5 σ_2 = 2.0	0.74	11.5	7.3

[a]The experimental data were fitted as the sum of two independent Gaussian functions. For the simulation only the width of the more populated one (here reported) was used.

Table B.3
Beam parameters used for the FLUKA simulation of the ^{10}C beam of 272 MeV/u in achromatic and mono-energetic mode. The standard deviation is here reported for all the quantities that were described with a single Gaussian distribution. In the cases where the beam spot shape was better described as a double Gaussian distribution, the weighting factors ($a_{1,2}$), mean values ($m_{1,2}$) and the standard deviations ($\sigma_{1,2}$) of the two Gaussian curves are reported.

		^{10}C 272 MeV/u mono-energetic mode		
Beam spot size x (cm)	Beam spot size y (cm)	$\Delta p/p$ (%)	Divergence x (mrad)	Divergence y (mrad)
3.7	0.8	0.13[a]	9.9	5.4

		^{10}C 272 MeV/u Achromatic mode		
Beam spot size x (cm)	Beam spot size y (cm)	$\Delta p/p$ (%)	Divergence x (mrad)	Divergence y (mrad)
a_1 = 0.76 m_1 = −0.3 σ_1 = 1.0 a_2 = 0.24 m_2 = −0.3 σ_2 = 3.0	a_1 = 0.76 m_1 = −0.7 σ_1 = 0.6 a_2 = 0.24 m_2 = −0.7 σ_2 = 1.7	0.45[a]	10.7	5.7

[a]The experimental data were fitted as the sum of two independent Gaussian functions. For the simulation only the width of the more populated one (here reported) was used.

Table B.4
Beam parameters used for the FLUKA simulation of the ^{10}C beam of 155 MeV/u in achromatic and mono-energetic mode. The standard deviation is here reported for all the quantities that were described with a single Gaussian distribution. In the cases where the beam spot shape was better described as a double Gaussian distribution, the weighting factors ($a_{1,2}$), mean values ($m_{1,2}$) and the standard deviations ($\sigma_{1,2}$) of the two Gaussian curves are reported.

		^{10}C 155 MeV/u mono-energetic mode		
Beam spot size x (cm)	Beam spot size y (cm)	$\Delta p/p$ (%)	Divergence x (mrad)	Divergence y (mrad)
3.8	1.2	0.24[a]	10.4	7.0

		^{10}C 155 MeV/u Achromatic mode		
Beam spot size x (cm)	Beam spot size y (cm)	$\Delta p/p$ (%)	Divergence x (mrad)	Divergence y (mrad)
a_1= 0.73 m_1= −1.3 σ_1= 1.8 a_2= 0.27 m_2= −0.1 σ_2= 4.2	a_1= 0.62 m_1= −0.6 σ_1= 0.9 a_2= 0.38 m_2= −0.2 σ_2= 1.8	0.74	10.1	6.9

[a]The experimental data were fitted as the sum of two independent Gaussian functions. For the simulation only the width of the more populated one (here reported) was used.

Appendix B. Beam parameters used for the ^{11}C and ^{10}C FLUKA simulations

See Tables B.1–B.4.

References

[1] M. Durante, K. Parodi, Radioactive beams in particle therapy: past, present, and future, Front. Phys. 8 (2020) 326.

[2] Y. Iseki, T. Kanai, M. Kanazawa, A. Kitagawa, H. Mizuno, T. Tomitani, M. Suda, E. Urakabe, Range verification system using positron emitting beams for heavy-ion radiotherapy, Phys. Med. Biol. 49 (2004) 3179.

[3] J. Llacer, A. Chatterjee, E. Alpen, W. Saunders, S. Andreae, H. Jackson, Imaging by injection of accelerated radioactive particle beams, IEEE Trans. Med. Imaging 3 (1984) 80–90.

[4] T. Pfuhl, F. Horst, C. Schuy, U. Weber, Dose build-up effects induced by delta electrons and target fragments in proton Bragg curves—measurements and simulations, Phys. Med. Biol. 63 (2018) 175002.

[5] A.J. Lomax, Myths and realities of range uncertainty, Br. J. Radiol. 93 (2020) 20190582.

[6] M. Durante, J. Debus, Heavy charged particles: does improved precision and higher biological effectiveness translate to better outcome in patients? in: Seminars in Radiation Oncology, Vol. 28, (2) Elsevier, 2018, pp. 160–167.

[7] M. Durante, J. Flanz, Charged particle beams to cure cancer: strengths and challenges, in: Seminars in Oncology, Vol. 46, Elsevier, 2019, pp. 219–225.

[8] H. Paganetti, Range uncertainties in proton therapy and the role of Monte Carlo simulations, Phys. Med. Biol. 57 (2012) R99.

[9] A.C. Kraan, Range verification methods in particle therapy: underlying physics and Monte Carlo modeling, Front. Oncol. 5 (2015) 150.

[10] K. Parodi, Vision 20/20: Positron emission tomography in radiation therapy planning, delivery, and monitoring, Med. Phys. 42 (2015) 7153–7168.

[11] A.-C. Knopf, A. Lomax, In vivo proton range verification: a review, Phys. Med. Biol. 58 (15) (2013) R131.

[12] S.P. Nischwitz, J. Bauer, T. Welzel, H. Rief, O. Jäkel, T. Haberer, K. Frey, J. Debus, K. Parodi, S.E. Combs, et al., Clinical implementation and range evaluation of in vivo PET dosimetry for particle irradiation in patients with primary glioma, Radiother. Oncol. 115 (2) (2015) 179–185.

[13] F. Pennazio, G. Battistoni, M.G. Bisogni, N. Camarlinghi, A. Ferrari, V. Ferrero, E. Fiorina, M. Morrocchi, P. Sala, G. Sportelli, et al., Carbon ions beam therapy monitoring with the INSIDE in-beam PET, Phys. Med. Biol. 63 (14) (2018) 145018.

[14] R. Augusto, J. Bauer, O. Bouhali, C. Cuccagna, C. Gianoli, W. Kozłowska, P. Ortega, T. Tessonnier, Y. Toufique, V. Vlachoudis, et al., An overview of recent developments in FLUKA PET tools, Phys. Medica 54 (2018) 189–199.

[15] C. Toramatsu, E. Yoshida, H. Wakizaka, A. Mohammadi, Y. Ikoma, H. Tashima, F. Nishikido, A. Kitagawa, K. Karasawa, Y. Hirano, et al., Washout effect in rabbit brain: in-beam PET measurements using ^{10}C, ^{11}C and ^{15}O ion beams, Biomed. Phys. Eng. Express 4 (2018) 035001.

[16] K. Parodi, A. Ferrari, F. Sommerer, H. Paganetti, Clinical CT-based calculations of dose and positron emitter distributions in proton therapy using the FLUKA Monte Carlo code, Phys. Med. Biol. 52 (2007) 3369.

[17] A. Mohammadi, H. Tashima, Y. Iwao, S. Takyu, G. Akamatsu, H.G. Kang, F. Nishikido, E. Yoshida, A. Chacon, M. Safavi-Naeini, et al., Influence of momentum acceptance on range monitoring of ^{11}C and ^{15}O ion beams using in-beam PET, Phys. Med. Biol. 65 (2020) 125006.

[18] M. Durante, P. Indelicato, B. Jonson, V. Koch, K. Langanke, U.-G. Meißner, E. Nappi, T. Nilsson, T. Stöhlker, E. Widmann, et al., All the fun of the FAIR: fundamental physics at the facility for antiproton and ion research, Phys. Scr. 94 (2019) 033001.

[19] M. Durante, A. Golubev, W.-Y. Park, C. Trautmann, Applied nuclear physics at the new high-energy particle accelerator facilities, Phys. Rep. 800 (2019) 1–37.

[20] D. Boscolo, D. Kostyleva, M.J. Safari, V. Anagnostatou, J. Äystö, S. Bagchi, T. Binder, G. Dedes, P. Dendooven, T. Dickel, et al., Radioactive beams for image-guided particle therapy: The BARB experiment at GSI, Front. Oncol. 11 (2021) 737.

[21] J. Pawelke, L. Byars, W. Enghardt, W. Fromm, H. Geissel, B. Hasch, K. Lauckner, P. Manfrass, D. Schardt, M. Sobiella, The investigation of different cameras for in-beam PET imaging, Phys. Med. Biol. 41 (1996) 279.

[22] B. Jakoby, Y. Bercier, M. Conti, M. Casey, B. Bendriem, D. Townsend, Physical and clinical performance of the mCT time-of-flight PET/CT scanner, Phys. Med. Biol. 56 (8) (2011) 2375.

[23] K. Parodi, W. Assmann, C. Belka, J. Bortfeldt, D.-A. Clevert, G. Dedes, R. Kalunga, S. Kundel, N. Kurichiyanil, P. Lämmer, et al., Towards a novel small animal proton irradiation platform: the SIRMIO project, Acta Oncol. 58 (10) (2019) 1470–1475.

[24] M. Nitta, G. Lovatti, M. Safari, T. Binder, H.G. Kang, S. Takyu, G. Dedes, T. Yamaya, P.G. Thirolf, K. Parodi, Design and detector development for an in-beam small animal PET scanner, in: Deutschen Gesellschaft Für Medizinische Physik, 2020, Stuttgart.

[25] T. Böhlen, F. Cerutti, M. Chin, A. Fassò, A. Ferrari, P.G. Ortega, A. Mairani, P.R. Sala, G. Smirnov, V. Vlachoudis, The FLUKA code: developments and challenges for high energy and medical applications, Nucl. Data Sheets 120 (2014) 211–214.

[26] A. Ferrari, J. Ranft, P.R. Sala, A. Fassò, FLUKA: A Multi-Particle Transport Code (Program Version 2005), CERN-2005-10, Cern, 2005.

[27] G. Battistoni, T. Boehlen, F. Cerutti, P.W. Chin, L.S. Esposito, A. Fassò, A. Ferrari, A. Lechner, A. Empl, A. Mairani, et al., Overview of the FLUKA code, Ann. Nucl. Energy 82 (2015) 10–18.

[28] G. Battistoni, J. Bauer, T.T. Boehlen, F. Cerutti, M.P. Chin, R. Dos Santos Augusto, A. Ferrari, P.G. Ortega, W. Kozłowska, G. Magro, et al., The FLUKA code: an accurate simulation tool for particle therapy, Front. Oncol. 6 (2016) 116.

[29] H. Geissel, P. Armbruster, K.H. Behr, A. Brünle, K. Burkard, M. Chen, H. Folger, B. Franczak, H. Keller, O. Klepper, et al., The GSI projectile fragment separator (FRS): a versatile magnetic system for relativistic heavy ions, Nucl. Instrum. Methods. Phys. Res. B. 70 (1992) 286–297.

[30] N. Angert, C. Schmelzer, The UNILAC, a variable energy linear accelerator for atomic ions of any mass, Kerntech 11 (1969) 690–695.

[31] M. Steiner, K. Blasche, H.-G. Clerc, H. Eickhoff, B. Franczak, H. Geissel, G. Münzenberg, K.-H. Schmidt, H. Stelzer, K. Sümmerer, Preliminary measurements of SIS-18 beam parameters, Nucl. Instrum. Methods. Phys. Res. A 312 (3) (1992) 420–424.

[32] J. Kurcewicz, F. Farinon, H. Geissel, S. Pietri, C. Nociforo, A. Prochazka, H. Weick, J. Winfield, A. Estradé, P. Allegro, et al., Discovery and cross-section measurement of neutron-rich isotopes in the element range from neodymium to platinum with the FRS, Phys. Lett. B (ISSN: 0370-2693) 717 (4) (2012) 371–375.

[33] R. Schneider, A. Stolz, Technical manual ionization chamber MUSIC80, 2000, https://www-win.gsi.de/frs/technical/frssetup/detectors/music80.

[34] R. Janik, A. Prochazka, B. Sitar, P. Strmen, I. Szarka, H. Geissel, K.-H. Behr, C. Karagiannis, C. Nociforo, H. Weick, M. Winkler, Time projection chambers with C-pads for heavy ion tracking, Nucl. Instrum. Methods. Phys. Res. A 640 (2011) 54–57.

[35] C. Scheidenberger, H. Geissel, M. Maier, G. Münzenberg, M. Portillo, G. Savard, P. Van Duppen, H. Weick, M. Winkler, M. Yavor, et al., Energy and range focusing of in-flight separated exotic nuclei–A study for the energy-buncher stage of the low-energy branch of the super-FRS, Nucl. Instrum. Methods. Phys. Res. B. 204 (2003) 119–123.

[36] H. Geissel, T. Schwab, P. Armbruster, J. Dufour, E. Hanelt, K.-H. Schmidt, B. Sherrill, G. Münzenberg, Ions penetrating through ion-optical systems and matter—non-liouvillian phase-space modelling, Nucl. Instrum. Methods. Phys. Res. A. 282 (1989) 247–260.

[37] D. Schardt, P. Steidl, M. Krämer, U. Weber, K. Parodi, S. Brons, Precision Bragg-Curve Measurements for Light-Ion Beams in Water, Vol. 373, GSI Scientific Report, 2007.

[38] F. Horst, D. Schardt, H. Iwase, C. Schuy, M. Durante, U. Weber, Physical characterization of 3He ion beams for radiotherapy and comparison with ^{4}He, Phys. Med. Biol. 66 (2021) 095009.

[39] H. Stelzer, B. Voss, Ionization chamber for ion beams and method for monitoring the intensity of an ion beam, 2002, Google Patents, U.S. Patent No. 6,437,513.

[40] V. Vlachoudis, et al., FLAIR: a powerful but user friendly graphical interface for FLUKA, in: Proc. Int. Conf. on Mathematics, Computational Methods & Reactor Physics, Vol. 176, M&C 2009, Saratoga Springs, New York, 2009.

[41] S. Seltzer, J. Fernandez-Varea, P. Andreo, P. Bergstrom, D. Burns, I. Krajcar Bronić, C. Ross, F. Salvat, Key Data for Ionizing-Radiation Dosimetry: Measurement Standards and Applications, ICRU Report 90, Oxford University Press, 2016.

[42] C. Kurz, A. Mairani, K. Parodi, First experimental-based characterization of oxygen ion beam depth dose distributions at the heidelberg ion-beam therapy center, Phys. Med. Biol. 57 (2012) 5017.

[43] F. Horst, W. Adi, G. Aricò, K.-T. Brinkmann, M. Durante, C.-A. Reidel, M. Rovituso, U. Weber, H.-G. Zaunick, K. Zink, et al., Measurement of PET isotope production cross sections for protons and carbon ions on carbon and oxygen targets for applications in particle therapy range verification, Phys. Med. Biol. 64 (2019) 205012.

[44] U. Weber, G. Kraft, Design and construction of a ripple filter for a smoothed depth dose distribution in conformal particle therapy, Phys. Med. Biol. 44 (1999) 2765.

[45] O. Tarasov, A. Villari, Fusion–fission is a new reaction mechanism to produce exotic radioactive beams, Nucl. Instrum. Methods. Phys. Res. B. 266 (2008) 4670–4673.